Review on Dynamic Stall Control in Airfoils

Abraham Adera(✉) and Siva Ramakrishnan

Department of Mechanical Engineering, Bahir Dar Institute of Technology, Bahir Dar University, Bahir Dar, Ethiopia
abraham1928adera@gmail.com, abrahama@bdu.edu.et, vsmpl967@yahoo.com

Abstract. Dynamic stall is a process that occurs when the angle of attack of airfoils exceeds the critical value which leads to fluctuation of aerodynamic loads and loss of performance of streamlined bodies like wind turbines and helicopters as a result of boundary layer separation. This review presents dynamic stall control methods in the oscillating airfoil. Airfoil shape modification and momentum blowing on a boundary layer were the focus of this paper. From the review, it was found that making the leading edge of an airfoil to change its shape dynamically, can help to alleviate dynamic stall in different flow conditions. Similarly, energizing the boundary layer of the flow by momentum blowing both steadily and unsteadily was found to be effective in dynamic stall control while the latter was superior. From the review, it was shown that whatever methods were applied to control dynamic stall, the effectiveness of those methods depend on other parameters too like reduced frequency.

Keywords: Airfoil shape · Angle of attack · Boundary layer · Dynamic stall · Momentum blowing

1 Introduction

Dynamic stall is a phenomenon which occurred when the angle of attack exceeds the critical value which leads aerodynamic loads to sharply vary as the boundary layer dynamically separates from the suction surface [1]. When AOA increases its value more than the static stall angle, an unsteady nonlinear phenomenon of dynamic stall occurs leading to shedding of flow separation at the airfoil surface followed by a higher loss of lift force and moment [2] as well as high - level noise [3]. It is characterized by series of fluid flow separations and reattachments which yield suction-side boundary layer separation and subsequent roll-up into a leading edge vortex, which is responsible to massive structural vibrations, lower efficiency, and unwanted noise [4]. This situation can occur on any lifting surface including but not limited to helicopters, highly maneuverable fighter jets and modern wind turbines as their angle of attack being above their normal static stall angle forcing to undergo pitching, flapping, and plunging or vertical translating movements series [5].

In helicopter forward flight, the normal velocity component with respect to ambient air at rest varies while the rotor covers one full revolution. Since there is high velocity (M = 0.9) at the tip of the blade, there will be a significant pressure difference between advancing and retreating blades as there is only very low velocity on the latter blade.

F. A. Zimale et al. (Eds.): ICAST 2018, LNICST 274, pp. 380–400, 2019.
https://doi.org/10.1007/978-3-030-15357-1_32

The sinusoidal pitching motion of retreating blade so as to bring the two pressure differences equal, makes the AOA to continually vary. This unsteady flow situation observed in helicopters causes vortices to develop at the leading edge which then shed in to wake. This causes flow separation that severely limits the flight envelop [6]. It is a function of airfoil geometry, the amplitude of oscillation, reduced frequency, Reynolds number, and the Mach number. Its overall stages are LEV at slightly higher AOA above static stall, full stall during shedding and flow reattachment [5, 7, 8].

The angle of attack variation in wind turbines is due to many reasons such as atmospheric turbulence, the earth boundary layer, the wakes of wind turbines located further upstream, tower shadow effects, yaw misalignment, wind shear and tower passage [9]. In VAWT, the blade velocity magnitude and direction, as well as the azimuthal angle of attack change continuously at low tip speed ratio due to complex flow regime created by the above - listed effects. To understand clearly why the angle of attack varies in wind turbines, let's refer to Fig. 1 adapted from [1] based on sinusoidal rotating HAWT. As shown in Fig. 1(a) in the absence of any wind gust, the wind speed is perpendicular to the rotor disc and is constant. In this case, the AOA will be constant. However, this is not the situation observed in the real operation of wind turbines. Wind gust causes the wind speed to increase and thus both AOA, and relative wind speed will vary from previous values, specifically increase, see Fig. 1(b). In yawed operation, the wind speed is not totally perpendicular to the rotor disc. When the blade moves towards the wind, Fig. 1(c), relative wind speed increment and AOA decrement happen and the opposite will happen when the wind moves away from the blade, Fig. 1(d). This causes the variation in AOA. The airfoil then will undergo an oscillatory motion with a turbine rotation frequency. This frequency, in most of the literature, given in terms of reduced frequency as, $Kred = \omega C/U\infty$. The sole effect of this situation in dynamic stall perspective is a LEV to develop and flow separation to shed on creating an additional vortex as it retreats to the trailing edge [1].

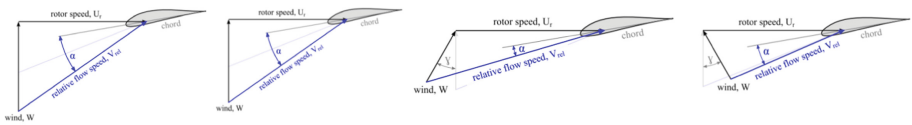

Fig. 1. Angle of attack variation in HAWT [1]

The variation of the angle of attack as the airfoil rotates can be obtained by referring Fig. 2 from [9]. Where VW = V∞ = free stream velocity, CN = normal force coefficient, θ = azimuth angle which will be zero when the blade becomes parallel and faces to the wind, CF = tangential force coefficient.

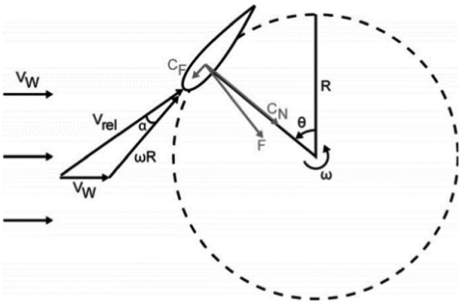

Fig. 2. Angle of attack variation in VAWT [9]

Vrel is the relative velocity induced as a result of blade rotation

$$\text{Vrel} = \left((\text{R}\omega)^2 + \text{V}\infty^2\right)^2 \tag{1}$$

$$Vrel = \sqrt{\left[(TSR + cos\theta)^2 + \sin^2\theta\right]}\,[9] \tag{2}$$

The variation of AOA as azimuthally angle varies is given as

$$AOA = \tan^{-1}\left(\frac{sin\theta}{TSR + cos\theta}\right)[10] \tag{3}$$

Having an understanding of the detrimental consequences of dynamic stall, many research works have been done on alleviating these negative effects. There are many techniques that can be applied to suppress the onset of the dynamic stall and totally reduce its adverse effects. These techniques broadly can be classified as active and passive techniques. Active flow techniques are state of the art and can be applied to any airfoil shape and geometry after some modification. However, active techniques are expensive and their implementation is cumbersome. While passive techniques are simple and cost wise, they are not fully efficient in an unsteady flow condition. For example, [10] applied three passive methods to control dynamic stall of the NACA0021 airfoil. Their control strategies were Leading - edge vortex generators to create counter-rotating stream wise-oriented vortices by using delta type leading edge vortex generators, generating counter-rotating span wise-oriented vortices by elevated wire and applying a cavity at the quarter-chord of the airfoil to act as a sink to the upstream moving vortex. However, all methods were found to delay the onset of vortex only at lower pitch rate. Additionally, vortex generators have a drag penalty while they can improve aerodynamic forces to some extent [11]. Due to this reason, this review paper will focus on active methods to control dynamic stall.

Amongst the many active methods seen in the literature, [1, 12] applied to a momentum fluid to energize the boundary layer so as to delay boundary layer separation and enhance the aerodynamic performance. In both of these studies, it was found

that blowing in an unsteady manner that follows the sinusoidal variation of the AOA was effective than constant blowing, especially at higher reduced frequencies. [6] applied navel concept of variably dropping the leading edge of the airfoil so as to improve the pressure distribution that causes flow separation and hence dynamic stall. Many other researchers worked on dynamically dropping the leading edge with the aim as that of [6]. Periodic surface morphing of the airfoil has also found to be the most effective way in reducing dynamic stall as per from [11].

Addition of free stream turbulence [13–15] on a flowing fluid in order to balance the internal turbulence of the fluid by external turbulence was found to be effective in reducing the fluctuations of aerodynamic loads. Energizing the boundary layer [9, 12] by giving high suction pressure in order to prevent flow separation which is the result of adverse pressure gradient was also ideal for suppression of dynamic stall. Redesigning methods, [6, 11], to get higher radius at the leading edge so as to delay separation by making it to travel more distance were also found to be an effective way of suppressing dynamic stall.

Wondering the unreserved efforts on studying dynamic stall control by using active techniques from previous researchers, from the knowledge of the authors, there has not been an attempt to review those active dynamic stall alleviating mechanisms as a single study except that performed by [16] on periodic excitation. Thus, the aim of the present paper is to study dynamic stall control techniques so as to separately study effects of different dynamic stall determining parameters like Reynolds number, reduced frequency, free stream velocity, Mach number, and turbulence effects. Since some authors focus on low Reynolds numbers while others on high, similarly the inconsistency of selecting the reduced frequency and Mach number among many researchers, the aim of this review paper is to bring those different parameters into one so that a reader can get many notes at various parameters in a single document. As a final note this review will focus on only momentum blowing and leading edge modification. Therefore, the reader should not be confused as the lists in the review were considered as the only active control methods.

The flow of this review paper is as follows. The paper starts with defining mathematically the adverse pressure gradient that is responsible for flow separation and then a review has been made on the overall dynamic stall process. Detailed discussions on airfoil shape modifications and the addition of momentum fluid as a means to control dynamic stall follow and then the conclusion has made.

2 Results and Discussion

2.1 Pressure Gradient and Lift

Pressure gradient: When the air moves aft from lower static pressure to trailing edge, adverse pressure gradient develops which causes flow transition from laminar to turbulent and the lower boundary layer to separate from the surface. This causes lift loss due to the loss of suction pressure along the chord by the airfoil. This is the sole effect observed in the dynamic stall. The pressure gradient as a function of tip speed ratio can be determined from [13].

Motion equation

$$\frac{Vr\partial Vr}{\partial r} = r\omega^2 - \frac{\partial P}{\rho \partial r} \tag{4}$$

In the above equation, r is the distance from the hub (in the case of the wind turbine), Vr is radial velocity (assumed to be constant), ω is angular velocity of blades and ρ is density. Rewriting the pressure term in terms of the coefficient of pressure, we can get the relation

$$\frac{Vr\partial Vr}{\partial r} = r\omega^2(1 - Cp - \left(v^2 \partial Cp\right)2\partial r \tag{5}$$

Assume Cp (pressure coefficient) is constant in the radial direction,

$$V^2\left(\frac{\partial Cp}{2\partial r}\right) = 0, \text{thus}, Vr = r\omega^2\sqrt{(1 - Cp)}$$

For totally stalled condition, Cp is of the order of −1 and hence $Vr = \sqrt{2r\omega}$

Therefore, $\left(\sqrt{2r\omega}\right)\partial\frac{\sqrt{2r\omega}}{\partial r} = r\omega^2 - r\omega^2 - \frac{\partial P}{\rho\partial r}$ and thus, the pressure gradient will be $\frac{\partial P}{\rho\partial\theta} = 2Vr\omega$

In terms of tip speed ratio, TSR, and radial position on the blade,

$$\frac{\partial Cp}{r\partial\theta} = \left(4\sqrt{2}\right)r^{0.5}\left(1 + \left(\left(\frac{R}{r}\right)TSR\right)^2\right)[14] \tag{6}$$

Lift: Since the angle of attack is continually changing in a dynamic stall situation, the lift gain and loss during the entire upstroke and downstroke motion are totally different and it is time-dependent. [17] conducted a dynamic stall model to determine wind turbine lift coefficient employing time delay fully attached and separated flow conditions with LE separation vortex and pressure peak contributions. According to them, lift starts dimensioning as TEV counteracts LEV and this dimensioning effect can be described by the following first order differential equation.

$$CL, v(t) + \omega 4Cl, v(t) = \left\{\begin{array}{l} \Delta Cl(t), for\ \alpha > 0\ and\ \alpha < 0 \\ 0\ for\ other\ conditions \end{array}\right\}[18] \tag{7}$$

Here CLv(t) is the actual value of the induced lift after the initiation of dimensioning effect and ω4 is a parameter that controls the dimensioning effect of vortex lift and α is the maximum angle of attack (Fig. 3).

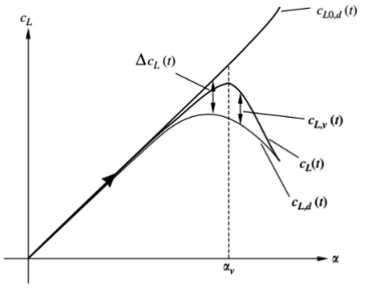

Fig. 3. lift versus angle of attack [17]

2.2 Overall Dynamic Stall Situation

[5] were able to show the whole dynamic stall process while simulating of NACA 0012 pitching airfoil at a Reynolds number of 105 as shown in Fig. 4. Formation and shedding of LEV which has low - pressure wave on the suction surface of the airfoil is a characteristic of the deep dynamic stall.

Upstroke motion: fluid flow is attached to the airfoil until it passes through some important angles of attack. This situation is shown from [−5°, 10°] by [5] until the creation of the LSB at 15.7° which then converted to LEV at about 20.6° causing thick reverse separation flow. Sudden lift increase observed from [5] at 22.5° which remained up to 23.86° where LEV gets peak by covering the whole airfoil surface. According to [18], LEV breaks down into two small counter - rotating vortices, showing LE boundary layer is unstable. However, this breakdown doesn't affect the attachment. TEV formed as LEV departs from the airfoil surface while traveling downstream. The situation is shown at 24.7° upstream from [5]. The creation of TEV is so as to satisfy Kelvin's circulation theorem, i.e. a TEV rotating in anti-clockwise fashion created in order to satisfy the conservation of circulation.

An airfoil at a high angle of attack creates an adverse pressure gradient on the upper surface that is too strong for the kinetic energy in the boundary layer to overcome. A Stall occurs when the boundary layer does not adhere to the surface near the leading edge. This occurs beyond Clmax AOA which causes a significant decrease in Cl. From [5] this can be observed at 25° up, where LEV becomes severe as it rolled on the upper surface which makes extraordinary complex flow on the upper surface. [19] were able to show the aerodynamic lift coefficient curve trend in a dynamic stall at K = 0.026 & Re = 106. Even if they employed high Reynolds number of 106 which can be considered turbulent region, their result will not affect description of flow topology of [5] who employed 105 Reynolds number. The reason is Reynolds number will not independently affect the flow and additionally, both laminar and turbulent flows have an almost the same aerodynamic trend. They compare their simulation result of the S809 airfoil at a reduced frequency of 0.026 to prior experimental and numerical works of their reference. They concluded that all trend of lift coefficient curve of the stationary airfoil is almost the same to the oscillating airfoil.

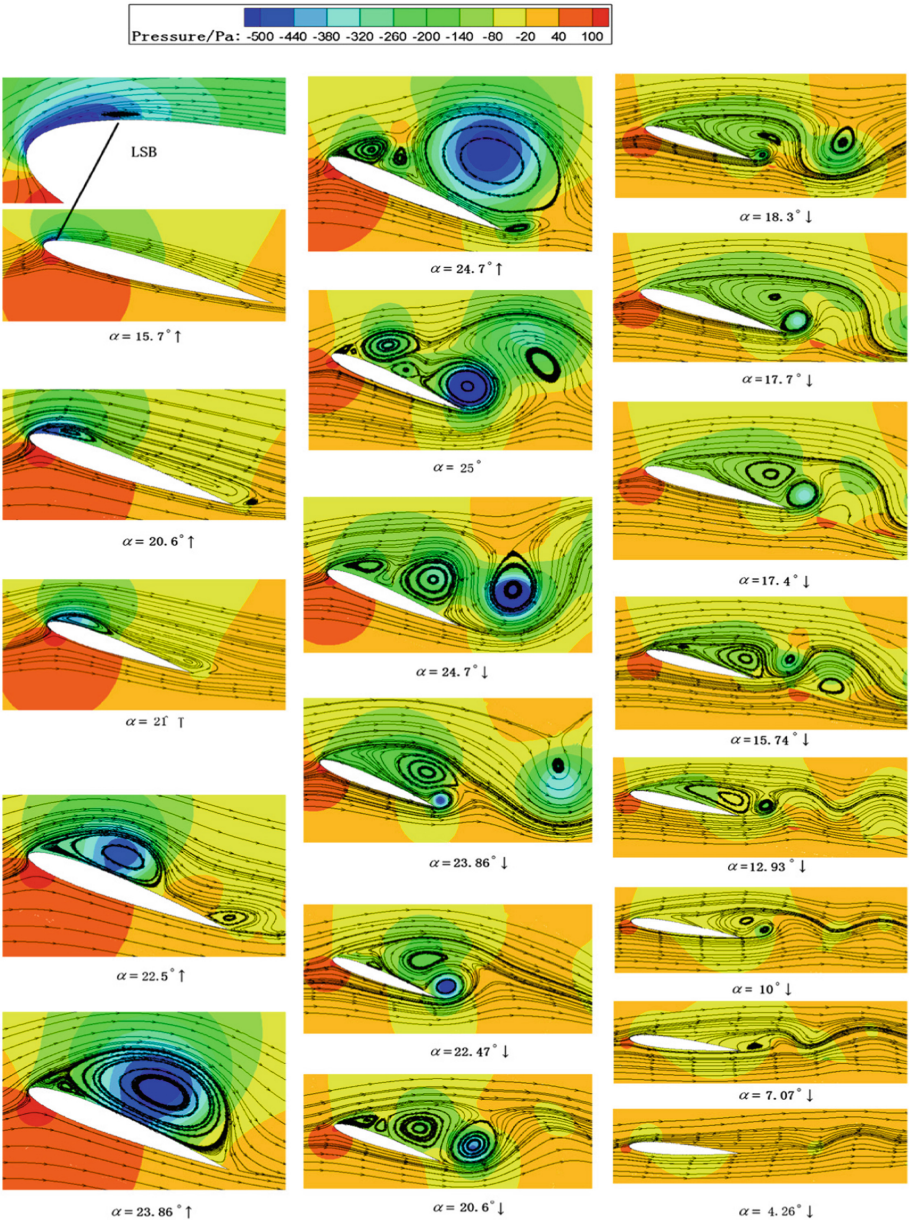

Fig. 4. Pressure field superimposed on the instantaneous streamlines [18]

Downstroke: it is during downstroke motion that small vortices created and merged to form a large vortex. [5] showed this at 24.7° down. After the shedding of the rolling up vortex, according to [14], higher magnitude induced re-circulated flow increases from TE in this downstroke motion causing TEV to push one big vortex obtained by

merging of smaller vortices at 23.86° [14]. TEV detaches exactly after passing 18.3° and after 15.74° onwards, merging of the upper surface vortex into one and then rolling of detached TEV continue to happen until 7.707° where flow reattachment occurs [5]. Generally, as we seen above, flow reverses from trailing edge and moves upstream towards leading edge and hence dynamic stall vortex formed when the shear layer lifts up as a result of the reversed flow.

3 Dynamic Stall Control

We can reduce the detrimental effect of the dynamic stall by carried out different strategies. Broadly speaking, dynamic stall suppression methods can be classified as active and passive methods. As we tried to discuss at the beginning, passive control techniques are simple and cost-effective yet they fail in alleviating dynamic stall for all components at all flow conditions. As per the literature we found from [11], passive control methods like trips and vortex generators are only effective in limited flow conditions i.e. they can improve aerodynamic coefficients at some conditions but they will bring drag penalty at other conditions. Also, boundary layer trips were found effective only if the flow separation point is fixed which is not always possible in unsteady flow situation. Based on this, in this paper, active flow control methods are discussed.

3.1 Airfoil Shape Modification

The shape of an airfoil has its own meaning in terms of aerodynamic performance of a helicopter or aircraft. Sharp leading edge of an airfoil can make air flow to accelerate on the upper surface. According to [20] the movement of air from stagnation point towards the suction peak at the upper surface downstream of the nose causes the flow to accelerate and this effect is enhanced by the sharp leading edge of the airfoil. This high acceleration can lead to local supersonic flow that will generate shock. Additionally, due to the relationships among pressure, force and acceleration, there will be a high adverse pressure gradient. Both of these effects can cause flow separation and dynamic stall. According to [6] local shape of the airfoil near the leading edge plays a major roll on the development of dynamic stall formation which helps us to consider changing the airfoil leading edge to reduce dynamic stall without affecting the lift generation. According to [21], increased leading edge radius can alleviate peak suction pressure and the adverse pressure gradient can be reduced by distributing low - pressure region to the airfoil upper surface by making the leading edge to have more rounded shape. Thus, modifying the shape of the leading edge can help to suppress of dynamic stall on the airfoil.

[20] provide a clear and detailed process of designing a dynamically deforming airfoil. The aim was to get an airfoil that adapts the dynamically changing flow situation observed in unsteady flow environment, especially for a helicopter airfoil. It is called dynamically deforming leading edge airfoil, DDLE. The airfoil was designed and manufactured from a 0.001- inch thick fiberglass inside and carbon fiber outside. 20% of its leading edge i.e. the distance from leading edge up to 0.2 C of the airfoil

was made from fiberglass. The disadvantage of metals of being yielded, too thin sheets, residual stress, and chemical milling forced him to use composite material for his work. The airfoil's leading edge deformation accomplished by a mandrel sandwiched between inner and outer surfaces. There was software driven motor equipped with an encoder and assisted by a PDI to record digital display of DDLE deformation. The synchronization among drive system, motion controller and drum camera of PDI were made by the sinusoidal oscillations of the airfoil and DDLE shape changes at different rates from various AOA. The DDLE airfoil deformation images were taken by PDI image plane and it is then traced to give new airfoil profiles. Each 0.003 in rearward leading edge displacement from the previous position gives a new single airfoil shape. The new generated airfoil shape given numbers with 0 means no change in shape. The details of designing and fabricating DDLE can be found in [20]. In [21] a dynamic shape adaptation method was applied experimentally for controlling dynamic stall at Mach number $M = 0.3, Kred = 0.0503$ for a NACA 0012 airfoil oscillating at $\alpha = \alpha o + 10\, sin\, \omega t$. The manufacturing and all working conditions were the same as seen above on [20]. The designed DDLE airfoil was alternately named SAP (shape adapting while pitching) and the results were validated against a fixed shape 8.5 airfoil. From the interferograms recorded using PDI (not shown), the flow fully attached for shape 2 and shape 7.5 until AOA reaches 16° which was much better than that of the NACA 0012 airfoil that shows the onset of dynamic stall earlier at 14° as the same Mach number of 0.3 revealing the advantage of dynamic shape changing. The result was the same for a fixed 8.5 shape airfoil too. A small number of fringes observed for shape 7.5 at 14 AOA indicate the dropping of peak suction though the flow remains attached to its leading edge. This was seen after a trailing edge separation occurred from AOA of 17° to 19° for shape 7. The reduction in peak suction has also observed in down stroke motion at 18 and 19 AOA for shape 7 followed by a light dynamic stall at AOA of 16° which has low severity for a full dynamic stall.

Figure 5 gives the change effects on vorticity flux though NACA 0012 airfoil did not include in Fig. 5 as it already stalls at 14° and complicated flow separation has occurred at 16°. As shown in Fig. 5, dynamically adapting SAP airfoil shows better vorticity distribution at AOA of 15° than that of the fixed 8.5 shape airfoil. However, the peak vorticity flux of SAP goes upstream from X/C = 0.08 to 0.05 and its value was not exceeding that of fixed 8.5airfoil. At further increase in AOA of 20°, the vorticity flux of the fixed 8.5 shape airfoil doubles that of SAP at X/C = 0.05 showing no dynamic stall vortex seen in the deforming case. During downstroke motion, SAP experiences slightly higher vortices than fixed 8.5 shapes. However, this slight increase in vorticity can give higher circulation that can add lift improvement. Having the decent conclusions and analysis from the work of [21], we don't notice at what shape types (how much displacement of the leading edge) of the SAP airfoil the improvements in Fig. 5 reached.

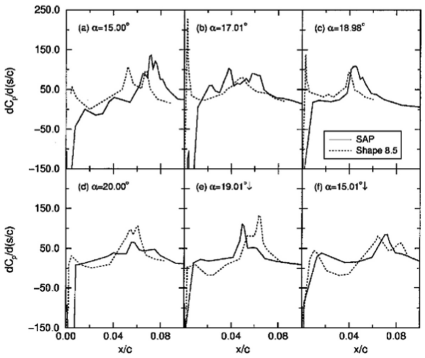

Fig. 5. Effect of shape change on vorticity flux development [21]

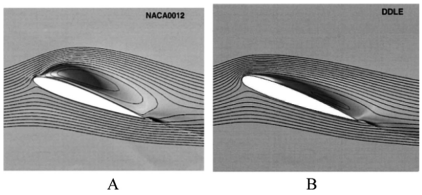

Fig. 6. Vortex distribution, AOA = 19.3° [22]

In [22], applying 2D Navier Stokes solver to define moving boundaries, they alleviated dynamic stall of NACA 0012 airfoil as compared from the surface pressure distribution and load hysteresis loops for NACA0012 or baseline airfoil. Curvilinear body fitted grid which is a system of interconnected springs from a 2D Navier Stoke solver was applied. The grid line was a tension spring connecting two consecutive grid points. The system worked such that the motion of the airfoil determines the motion of grid nodes. The magnitude of grid motion was determined by the spring stiffness value.

As shown on Fig. 6a, due to the leading edge vortex there was separation and recirculation on the upper surface of NACA 0012 airfoil at 19.43° upstroke. However, the smaller separation thickness of DDLE implied the suppression of LEV. This LEV sheds at 20° upstroke giving a decrease of the suction peak that is a sign of lift loss. However, the DDLE airfoil will start dynamic stall at this time. The DDLE airfoil gradually attaches to the boundary layer and its separation point moves to TE. In contrast the NACA0012airfoil, DDLE airfoil experiences a secondary vortex shedding which differentiates the two airfoils during down stroke. Keeping the other parameters same, at higher Mach number of 0.4, shock-induced flow separation found to cause the dynamically changing airfoil to experience dynamic stall during upstroke and a secondary vortex during down stroke. Thus, the DDLE airfoil will not good at high Ma.

Another interesting research on dynamic stall study using a deformable leading-edge concept was done by [6]. In this work, the start of deformation was designated by φ, the phase angle of pitch motion in cyclic pitch such that the leading edge starts to drop at point A where phase angle increases to φdef. The maximum drop amplitude corresponds to the maximum value of overall AOA at point B as φ further increases to $\frac{\pi}{2}$. Further moving of φ to the right leads the beginning of the rise of the leading edge

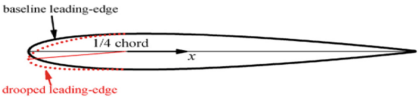

Fig. 7. VDLE airfoil [6]

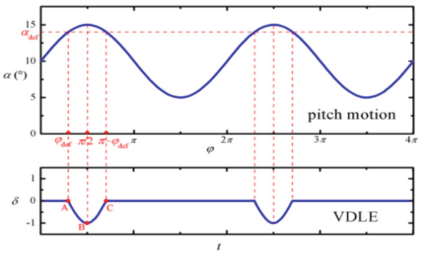

Fig. 8. VDLE mechanism [6]

until the airfoil recovers its shape at which the deformation ends and the rigid airfoil continues to pitch, see Figs. 7 and 8.

The process of dropping the leading edge in the region between A & c was defined a half period of sinusoidal wave given as

$$\omega def = \omega(\pi/(\pi - 2\varphi def))$$

Thus for one period of airfoil pitching motion, each point on the first quarter chord of the deforming edge is

$$\delta(x,t) = \left\{ \begin{array}{c} -A(x)\sin\left[\omega def\left(t - \frac{\varphi def}{\omega}\right)\right], \frac{\varphi def}{\omega} < t < \frac{\pi - \varphi def}{\omega} \\ 0, otherwise \end{array} \right\}, [6] \tag{8}$$

Where, $A(x) = Al * \frac{C}{4} X^n$ and $X = |x|/\left(\frac{c}{4}\right)$, X is non dimensionalized x coordinate. Control parameters were Al, n, and φ which determine respectively amplitude of drop of leading edge, the closeness of deformation to the leading edge point and how long the drop will take to begin. Thus, for mode 1 Al varies from 0.01, 0.5, to 0.1, n from 1.5 to 5 and φ from 0.2π, 0.3π, 0.35π to 0.4π and the test cases for mode two were a range of φ from 0.2π, 0.3π to 0.35π; and a special case of stationary leading edge.

Figure 9 shows how VDLE improves the lift, drag and moment coefficients by 61%, 69%, and 81% respectively for three different droop amplitudes at 0.2π. Additionally, we can easily observe that keeping π constant, increasing droop amplitude means improving the hysteresis loops of lift and drag. This can be seen by comparing Fig. 9B which shows attached flow with no vortex of the VDLE airfoil to that of

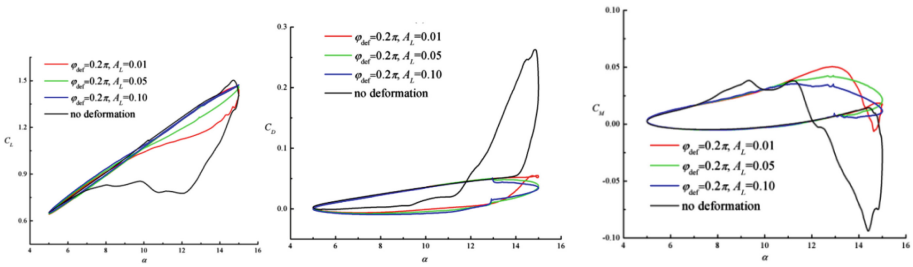

Fig. 9. Aerodynamic coefficients [6] at $\varphi def = 0.2\pi$

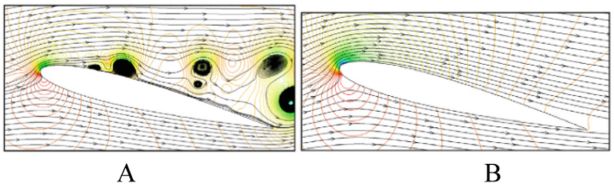

Fig. 10. Flow field improvement at a = 13.42 down stroke A. baseline B. VDLE at $\varphi def = 0.2\pi, Al = 0.05, n = 1.5$[6]

baseline at Fig. 9A. The same situation was observed for 3π except flow separation and instability of flow as Al is bigger (Fig. 10).

Changing n from 1.5 to 5 (making the distribution of deformation more to the leading edge) at the same deformation location improves aerodynamic loads and delays flow separation. This is because in an airfoils pitching motion dynamic stall and flow separation mostly happen from the leading edge which then distributes to the remaining part. From Fig. 11 we can observe that increasing the value of Al has the same meaning as increasing n as the concentration of droop deformation and amplitude of droop really

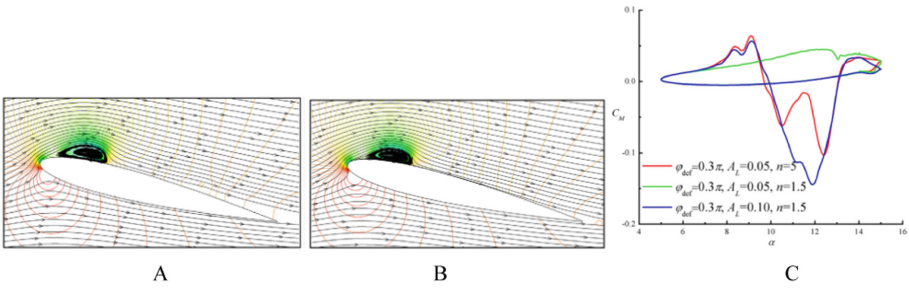

Fig. 11. A and B streamline and pressure counters at 13.42 AOA downstream A. $\varphi def = 0.3\pi, Al = 0.05, n = 5$, B. $\varphi def = 0.3\pi, Al = 0.1, n = 1.5$ C. pitching moment [6]

matter on dynamic stall control. However, this situation brings a bigger nose-down pitching moment that is a limitation for this assumption, see Fig. 11c.

To this end, we have seen two - dimensional airfoils in dynamic stall control. However, very few researches have been carried out to show how dynamic stall looks like in three - dimensional shape of the airfoil. [23] performed a dynamic stall control method that combines both two dimensional and three - dimensional effects. In their work, they used both the CFD method and a new optimal or Sequential Quadratic Programming (SQP) method with a new linear search strategy. In the numerical method, they generated a C O topology 3D rotor blade which employs geometric

conservation law in order to prevent errors due to the deformed grid. The aim of using SQP was to reduce the computational cost of aerodynamic load simulation by working with many constraints at a time. Constraint optimization problem and design functions are respectively given as

$$\{\min f(x)\ ands.tci(x) \geq 0, i = 1, 2, \ldots, m\}, [24] \tag{9}$$

$$x^{new} = x + tsd, [24] \tag{10}$$

Where $x = x1, x2, \ldots, xn$ are design variable obtained from airfoil parameters used to design the new airfoil, $d = d1, d2, \ldots, dn$ is search direction, ts is step size.

Their optimization procedure employs 12 design variables so as to fit the geometry of the airfoil based on OA209 airfoil and the final shape of the optimized airfoil is shown in fig below with blue color which has larger leading edge radius as compared to the original OA 209 airfoil.

Rotor airfoil in its forward flight situation experiences dynamic stall on its retreating side between 0.7R to 1.0R. This shows that a helicopter rotor airfoil works

Table 1. Design points of [23]

2D case		3D case	
Design point 1 $M = 0.3$ $K = 0.07$ $\alpha = 10 \pm 6$	Design point 2 $M = 0.4$ $K = 0.05$ $\alpha = 8 \pm 6$	Forward flight Advance ratio = 0.344 Cyclic pitch, $\theta = 12.55° + 1.92\cos\omega t - 6.94\sin\omega t$ Flapping angle, $\beta = 2.85° - 0.14\cos\omega t + 0.34\sin\omega t$	Hover $M = 0.626$ Advance ratio = 0 Pitch angle $\alpha = 12 - 6\sin\omega t$

under various Mach numbers, reduced frequencies, and angles of attack. So as to account these working conditions, [23] select two design points as given on the Table 1.

Based on the design point 1, time-varying aerodynamic loads are compared between the optimized and baseline airfoil in Fig. 12. The hysteresis loop of Cl of OA209 airfoil was found wider than that of the optimized airfoil which means flow

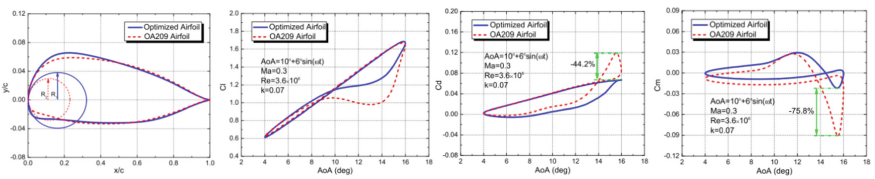

Fig. 12. A. Optimized vs. baseline airfoil, B, C, and D aerodynamic force improvement under design point 2 [23]

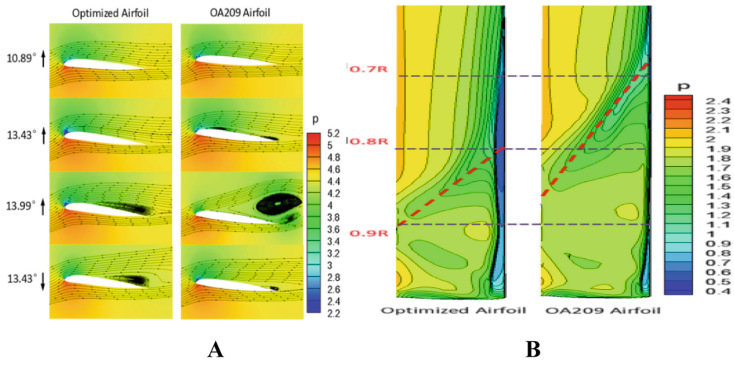

Fig. 13. Comparisons on A. Vortex development, B. nondimensional pressure in hover [23]

reattachment was achieved at very small AOA during the downstroke and thus light stall occurs. See Fig. 12B, C, D.

Under design point 2, Fig. 13A shows the alleviation of the dynamic stall as the vortex was already shed at 13.99° upstroke for the baseline, while it remains small at the same AOA and streamlines are almost attached to the boundary for the optimized cases. Figure 12B also shows the non-dimensional pressure distribution at 270° phase angle the region from 0.68R to 0.85R in the case of baseline airfoil and from 0.8R to 0.9R which is very narrow for optimized are affected by the LEV.

Under design point three - dimensional rotor condition, a new rectangular rotor based on SA349/2 helicopter rotor was designed with $Ma = 0.626$, $\alpha = 12 - 6\sin\omega t$ at a 0.75R location.

Figure 14 shows the pressure coefficients at different azimuth angles at 0.7R of the two airfoils. As shown in Fig. 14A and B, the adverse pressure gradient of the optimized airfoil was found lower than baseline OA209 airfoil. In Fig. 14C even if the

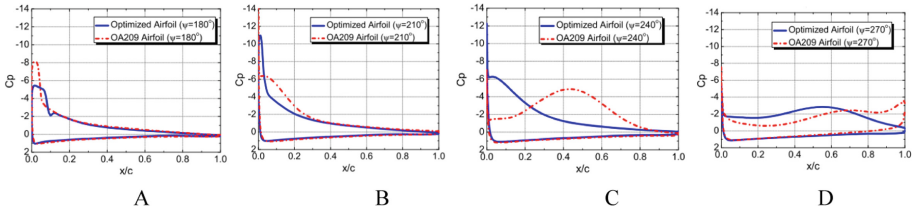

Fig. 14. Pressure coefficient in forward flight [23]

adverse pressure gradient of the optimized airfoil leads the baseline near the leading edge, it is less disturbed and comes to smaller value at 270°.

3.2 Boundary Layer Control by Blowing

Viscous layers show different properties as the airfoil oscillates. This causes the boundary layer to separate at one position while it will remain attached to the other.

Dynamic stall can be reduced and consequently lift can be increased if the boundary layer is energized so as to counteract the high-pressure gradient. Energizing can be carried out by adding high momentum fluid to the boundary layer. This will help the boundary layer to adhere to the airfoil at a higher angle of attack and the process is called boundary layer control.

In tangential blowing steady applying of the jet was found to be less effective since the amount of jet employed was constant for varying boundary layer interaction. However, periodically varying blowing follows the boundary layer movement and hence the idea is to add a strong jet to the boundary that tends to separate and weak jet to that less susceptible to separation. Both steady and unsteady blowing techniques were studied in [12] and are summarized in this review.

Boundary conditions and assumptions were; the jet nozzle is convergent, 1D and isentropic slot exit.

At the inflow boundary, the velocity components and temperature were specified as free stream conditions while the pressure is extrapolated from the interior. At the outflow boundary, the pressure was set equal to the free-stream static pressure and the velocity and temperature were extrapolated from the interior. Along the grid cut-line, periodic boundary conditions were enforced. On the airfoil surface (except for the slot exit), adiabatic, impermeable wall and no-slip boundary conditions were applied.

With these assumptions and for a given jet total pressure, Pt, and temperature, Tt, assuming known pressure at the slot exit, Pi, other quantities found as:

$$Tj = Tt\left[\frac{Pj}{Pt}\right]^{(\gamma-1)/\gamma}, [13] \tag{11}$$

$$Uj = \frac{\sqrt{2\gamma R}}{(\gamma-1)} Tt\left[1 - \left(\frac{Pj}{Pt}\right)^{\frac{\gamma-1}{\gamma}}\right], [13] \tag{12}$$

For unsteady blowing neglecting dynamic inflow effects, the equation can be redefined as

$$Tj = Tt(t)\left[\frac{Pj(t)}{\mathrm{Pr}(t)}\right]^{(\gamma-1)/\gamma}, [13] \tag{13}$$

$$Uj = \frac{\sqrt{2\gamma R}}{(\gamma-1)} Tt(t)[1 - \left(\frac{Pj(t)}{\mathrm{Pr}(t)}\right)^{\frac{\gamma-1}{\gamma}}, [13] \tag{14}$$

And unsteady total pressure,

$$Pt = Pts + \Delta Pt + \Delta Ptcos(\omega t + \phi)[13] \tag{15}$$

Where Tj and Uj are free stream temperature and velocity of the jet at slot exit inlet, Pj is pressure obtained by extrapolation of the flow pressure near the slot exit. The instantaneous total pressure Pr (t), total temperature Tt (t) and exit pressure (t) are used in the above formulas. A jet momentum coefficient was defined as:

$$C\mu = \frac{mVjet}{\frac{1}{2}\rho\infty V\infty^2 C}, [13] \tag{16}$$

Where $m = \rho jUjh$, h = slot hight and Vj is reference velocity of the jet assumed to flow isentropically to the free stream. For unsteady blowing, the momentum coefficient

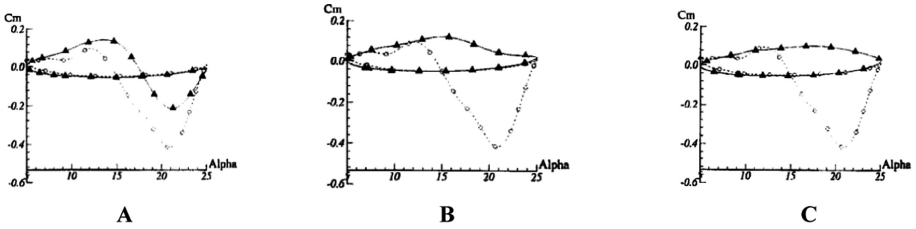

Fig. 15. Moment coefficient for NACA0012 at steady blowing in k = 0.25, momentum coefficient at (A. 0.05, B. 0.07, C. 0.09) [12]

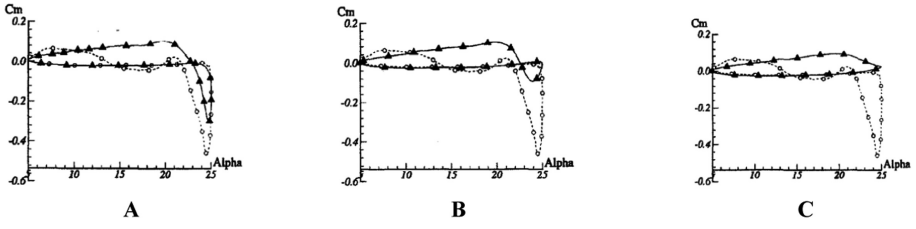

Fig. 16. Moment coefficient for NACA0012 at steady blowing in k = 0.15, momentum coefficient at (A. 0.05, B. 0.07, C. 0.09), ○ baseline, △ blowing [12]

variation was defined as

$$C\mu - \Delta C\mu \leq C\mu \leq C\mu + \Delta C\mu \tag{17}$$

The specification is: airfoil NACA0012 pitching at its quarter chord, motion $15^\circ + 10^\circ sin\,\omega$, $Re = 10^6$, $M = 0.2$, $K = 0.15, K = 0.25$, where $K = \frac{\frac{1}{2}\omega C}{V\infty}$

On Fig. 15 the effect of steady blowing is shown in terms of pitch moment coefficients. From the fig, it is shown that steady blowing was effectively suppressed nose down pitch moment especially at high momentum coefficients. On Fig. 16 for k = 0.15, until momentum coefficient reaches 0.09, the effect of blowing was not significant as there are pitching moment bouncing though a little reduction in the hysteresis loop was revealed. However, at 0.09, the positive impact of steady blowing on reducing nose down pitching moments was very satisfactory as those obtained at 0.07,0.09 at K = 0.25. Hence, in addition to the comparison of blowing at higher momentum coefficients, it can be understood that higher reducing frequency tends to suppress undesired moment coefficients. Other aerodynamic coefficients were also shown similar improvement at [12]. Additionally, as per flow structures (not shown here), blowing at higher momentum coefficient brings dynamic stall suppression except at 0.05 at which the improvement was not satisfactory.

Unsteady Blowing. The idea is varying the blowing strength following the AOA variation. The motion of the airfoil was kept the same as that used for steady blowing for comparison purpose.

The unsteady Pt was controlled to maintain the change in momentum coefficient a value 0.015%. Unsteady blowing was found to be effective as it gives very satisfactory result in suppressing flow separation from the airfoil. Flowing at an average Cμ of 0.05 (not shown) was comparable to steady blowing at Cμ = 0.07 showing effectiveness of the periodically varying blowing. The cases at higher average Cu (not shown) are also well noticed in improving dynamic stall better than constant blowing. Figure 17 elaborates this illustration more clearly at a phase shift of [−30, 30] at k = 0.25 at which the control was not satisfactory in other phases. Though the control was less effective relative to that at higher k, k = 0.15 also gives better control result than steady blowing [12].

Just like [1, 12] applied unsteady blowing on an oscillating airfoil. Control jet velocity-time profile was generated by supplying a voltage signal of the blowing to the mass flow controller. Phase-averaged lift coefficient was found from instantaneous lift coefficient which was calculated from instantaneous surface pressure distribution.

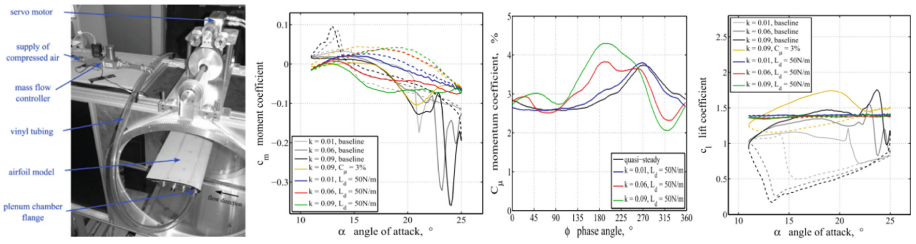

Fig. 17. Adaptive blowing (A), phase averaged lift and moment coefficients (B&C), momentum coefficient (D) [1]

$$Cl(\emptyset) = \frac{1}{N}\sum_{i=1}^{N} Cli(\emptyset), [1] \tag{18}$$

Mass flow controller regulates control jet speed to yield timed variation of $C\mu$. A compressed air at a temperature range of [295.5, 298] was supplied to a pressure vessel to give constant pressure upstream of the mass flow controller which was connected to leading edge plenum chamber, see Fig. 17 A. $C\mu$ was found from phase averaged wind tunnel speed $U\infty(\emptyset)$ and control jet speed $Uj(\emptyset)$. Phase averaged control jet speed $Uj(\emptyset)$ can be found from instantaneous volume flow rate $v(\phi)$.

$$Uj(\phi) = Uj, v = v(\phi)/sh[1] \tag{19}$$

This value is then normalized by the ratio of average jet speed to average phase averaged jet speed. The aim was to get the appropriate relationship between minimum lift per unit span and control jet momentum flux. The base for load control in adaptive blowing was a quasi-steady state. From the quasi-steady blowing, it was found that steady blowing at Cu of 2% has given a change in lift coefficient of 0.5 between AOA of 11 and 25° respectively. Based on this, an adaptive blowing was applied where finding minimum Cl was possible. This situation was found at momentum coefficient of 0.5% and 0.8% for an angle of attacks of 11° & 18° and 25° respectively. First $\alpha(\phi)$ and $U\infty(\emptyset)$ were found and then lift coefficient as a function of momentum coefficient were found by interpolating experimental results by phase. From the lift coefficient, the lift per unit span $\mathrm{Ld}(\phi)$ can be found which can be better used for calculating steady state phase averaged momentum coefficient time profiles as an input for adaptive blowing. As shown on Fig. 17, steady blowing at momentum coefficient of 3% was effective in eliminating dynamic stall vortex. Having this, varying momentum coefficient to adapt a constant lift per unit span of 50 N/m was carried out at various reduced frequencies especially at k = 0.09 which is very close to the value for wind turbines at a corresponding momentum coefficient profile that, Fig. 17D.

4 Nomenclature

Latin symbols

2D	two dimensional
3D	three dimensional
Al	amplitude of deformation
AOA	angle of attack
CFD	computational fluid dynamics
DDLE	dynamically deformed the leading - edge
HAWT	horizontal axis wind turbine
LEV	leading-edge vortex
NACA	national advisory committee for aeronautics
SAP	shape changing while pitching
SQP	sequential quadratic programming

TEV	trailing edge vortex
TSR	tip speed ratio
VAWT	vertical axis wind turbine
VDLE	variable drop leading edge
C	chord
$C\mu$	momentum coefficient
Cl	lift coefficient
CLd(t)	dimensioned lift
CLv(t)	actual value of induced lift after dimensioning
$Cl(\emptyset)$	phase averaged lift coefficient
$Cli(\emptyset)$	instantaneous lift coefficient
Cd	drag coefficient
CF	tangential force coefficient
Cm	moment coefficient
CN	normal force coefficient
Cp	pressure coefficient
d	search direction
h	slot height
K	reduced frequency

Greek symbols

ω	angular speed of the blade
ω_4a	parameter that controls the dimensioning effect of vortex lift
α	angle of attack
αv	critical angle at which the leading edge vortex detaches from the leading edge
$\emptyset$	phase angle
θ	pitch angle
ψ	phase angle
ρ	density
λ	tip speed ratio
φ def	starting point of deformation
Tj	free stream temperature of the jet at slot exit inlet
ts	step size
Tt	jet total temperature
$U\infty$	free stream speed
$U\infty(\emptyset)$	phase averaged wind tunnel speed
Uj	free stream velocity of jet at slot exit inlet
$Uj(\emptyset)$	control jet speed
$v(\phi)$	volume flow rate
Vi	reference velocity
Vr	radial velocity
Vrel	induced relative velocity
X	design variable
X/C	location from leading edge

Ld	lift per unit span
m	meter
M	mach number
Ma	mach number
N	Newton
P	Pressure
Pi	pressure at the slot exit
Pj	the extrapolated pressure at the slot exit
Pt	jet total pressure
R	radius
r	radial distance from hub
Re	Reynolds number
t	time

5 Conclusion

Dynamic stall control in oscillating airfoils was discussed. Airfoil shape modification especially at the leading edge and energizing the boundary layer by adding momentum fluid were the focus of this review. In order to make any modifications on an airfoil it is better to make attached flow as a basis. This can help us to reconsider the different arrangement of design parameters like Reynolds number, Mach number, and free stream velocity so that we will be able to arrive at the selection of best strategies that help us to suppress dynamic stall at a different angle of attack. Hover motion with both pitching and flapping motion, the effect of varying rate of change of airfoil deformation in dynamic stall control and further studying in reducing negative pitch down moment in VDLE might be the objective of the future researcher. In momentum blowing, the instability caused by increasing deformation amplitude and φ def at the same time and the combined use of constant and periodic momentum at a higher reduced frequencies and higher Mach numbers might also be a future idea.

Acknowledgment. This work acknowledged professor Siva & Dr. Shoeb for giving their helpful comments.

References

1. Müller-Vahl, H.F., Nayeri, C.N., Paschereit, C.O., Greenblatt, D.: Dynamic stall control via adaptive blowing. Renew. Energy **97**, 47–64 (2016)
2. Almohammadi, K.M., Ingham, D.B., Ma, L., Pourkashanian, M.: Modeling dynamic stall of a straight blade vertical axis wind turbine. J. Fluids Struct. **57**, 144–158 (2015)
3. Laratro, A., Arjomandi, M., Kelso, R., Cazzolato, B.: A discussion of wind turbine interaction and stall contributions to wind farm noise. J. Wind Eng. **127**, 1–10 (2014)
4. Buchner, A., Lohry, M.W., Martinelli, L., Soria, J., Smits, A.J.: Dynamic stall in vertical axis wind turbines: comparing experiments and computations. J. Wind Eng. **146**, 163–171 (2015)
5. Wang, S., Ingham, D.B., Ma, L., Pourkashanian, M., Tao, Z.: Turbulence modeling of deep dynamic stall at relatively low Reynolds number. J. Fluids Struct. **33**, 191–209 (2012)

6. Niu, J., Lei, J., Lu, T.: Numerical research on the effect of variable droop leading-edge on oscillating NACA 0012 airfoil dynamic stall. Aerosp. Sci. Technol. **72**, 476–485 (2018)
7. Li, Q., Maeda, T., Kamada, Y., Hiromori, Y., Nakai, A., Kasuya, T.: Study on stall behavior of a straight-bladed vertical axis wind turbine with numerical and experimental investigations. J. Wind Eng. **164**, 1–12 (2017)
8. Geissler, W., van der Wall, B.G.: Dynamic stall control on flapping wing airfoils. Aerosp. Sci. Technol. **62**, 1–10 (2017)
9. Yen, J., Ahmed, N.A.: Enhancing vertical axis wind turbine by dynamic stall control using synthetic jets. J. Wind Eng. Ind. Aerodyn. **114**, 12–17 (2013)
10. Choudhry, A., Arjomandi, M., Kelso, R.: Methods to control dynamic stall for wind turbine applications. Renew. Energy **86**, 26–37 (2016)
11. Jones, G., Santer, M., Debiasi, M., Papadakis, G., Debiasi, M., Papadakis, G.: Control of flow separation around an airfoil at low Reynolds numbers using periodic surface morphing. J. Fluids Struct. **76**, 536–557 (2018)
12. Sun, M., Sheikh, S.R.: Dynamic stall suppression on an oscillating airfoil by steady and unsteady tangential blowing. Aerosp. Sci. Technol. **3**(6), 355–366 (1999)
13. Sicot, C., Devinant, P., Loyer, S., Hureau, J.: Rotational and turbulence effects on a wind turbine blade. Investigation of the stall mechanisms. J. Wind Eng. Ind. Aerodyn. **96**(8–9), 1320–1331 (2008)
14. Hand, B., Kelly, G., Cashman, A.: Numerical simulation of a vertical axis wind turbine airfoil experiencing dynamic stall at high Reynolds numbers. Comput. Fluids **149**, 12–30 (2017)
15. Kim, Y., Xie, Z.-T.: Modelling the effect of freestream turbulence on dynamic stall of wind turbine blades. Comput. Fluids **129**, 53–66 (2016)
16. Greenblatt, D., Wygnanski, I.J.: The control of flow separation by periodic excitation, vol. 36 (2016)
17. Larsen, J.W., Nielsen, S.R.K., Krenk, S.: Dynamic stall model for wind turbine airfoils. J. Fluids Struct. **23**(7), 959–982 (2007)
18. Wang, S., Ingham, D.B., Ma, L., Pourkashanian, M., Tao, Z.: Numerical investigations on dynamic stall of low Reynolds number flow around oscillating airfoils. Comput. Fluids **39** (9), 1529–1541 (2010)
19. Gharali, K., Johnson, D.A.: Dynamic stall simulation of a pitching airfoil under unsteady freestream velocity. J. Fluids Struct. **42**, 228–244 (2013)
20. Chandrasekhara, M.S., Carr, L.W., Wilder, M.C., Paulson, G.N.: Design and development of a dynamically deforming leading edge airfoil for unsteady flow control
21. Chandrasekhara, M.S., Wilder, M.C., Carr, L.W.: Compressible dynamic stall control using dynamic shape adaptation. AIAA J. **39**(10), 2021–2024 (2001)
22. Sahin, M., Sankar, L.N., Chandrasekhara, M.S., Tung, C.: Dynamic stall alleviation using a deformable leading edge concept-a numerical study. J. Aircr. **40**(1), 77–85 (2003)
23. Wang, Q., Zhao, Q.: Rotor airfoil profile optimization for alleviating dynamic stall characteristics. Aerosp. Sci. Technol. **72**, 502–515 (2018)